REPORT DOCUMENTATION PAGE

Form Approved OMB NO. 0704-0188

1. REPORT DATE (DD-MM-YYYY)	2. REPORT TYPE	3. DATES COVERED (From - To)
	New Reprint	-

4. TITLE AND SUBTITLE	5a. CONTRACT NUMBER
Electronic band structures and optical properties of type-II superlattice photodetectors with interfacial effect	W911NF-10-1-0524
	5b. GRANT NUMBER
	5c. PROGRAM ELEMENT NUMBER
	611103

6. AUTHORS	5d. PROJECT NUMBER
Peng-Fei Qiao, Shin Mou, Shun Lien Chuang	
	5e. TASK NUMBER
	5f. WORK UNIT NUMBER

7. PERFORMING ORGANIZATION NAMES AND ADDRESSES	8. PERFORMING ORGANIZATION REPORT NUMBER
University of Illinois - Urbana Board of Trustees of the University of Illinois 1901 S First Street Champaign, IL　61820　-7473	

9. SPONSORING/MONITORING AGENCY NAME(S) AND ADDRESS(ES)	10. SPONSOR/MONITOR'S ACRONYM(S)
U.S. Army Research Office P.O. Box 12211 Research Triangle Park, NC 27709-2211	ARO
	11. SPONSOR/MONITOR'S REPORT NUMBER(S)
	58141-EL-MUR.13

12. DISTRIBUTION AVAILIBILITY STATEMENT

Approved for public release; distribution is unlimited.

13. SUPPLEMENTARY NOTES

The views, opinions and/or findings contained in this report are those of the author(s) and should not contrued as an official Department of the Army position, policy or decision, unless so designated by other documentation.

14. ABSTRACT

The electronic band structures and optical properties of type-II superlattice (T2SL) photodetectors in the mid-infrared (IR) range are investigated. We formulate a rigorous band structure model using the 8-band k · p method to include the conduction and valence band mixing. After solving the 8×8 Hamiltonian and deriving explicitly the new momentum matrix elements in terms of envelope functions, optical transition rates are obtained through the Fermi's golden rule under various doping and injection conditions. Optical measurements on T2SL

15. SUBJECT TERMS

Multiple quantum well, Photodetectors, Detector materials

16. SECURITY CLASSIFICATION OF:			17. LIMITATION OF ABSTRACT	15. NUMBER OF PAGES	19a. NAME OF RESPONSIBLE PERSON
a. REPORT	b. ABSTRACT	c. THIS PAGE			Shun Chuang
UU	UU	UU	UU		19b. TELEPHONE NUMBER
					217-721-3031

Report Title

Electronic band structures and optical properties of type-II superlattice photodetectors with interfacial effect

ABSTRACT

The electronic band structures and optical properties of type-II superlattice (T2SL) photodetectors in the mid-infrared (IR) range are investigated. We formulate a rigorous band structure model using the 8-band $k \cdot p$ method to include the conduction and valence band mixing. After solving the 8×8 Hamiltonian and deriving explicitly the new momentum matrix elements in terms of envelope functions, optical transition rates are obtained through the Fermi's golden rule under various doping and injection conditions. Optical measurements on T2SL photodetectors are compared with our model and show good agreement. Our modeling results of quantum structures connect directly to the device-level design and simulation. The predicted doping effect is readily applicable to the optimization of photodetectors. We further include interfacial (IF) layers to study the significance of their effect. Optical properties of T2SLs are expected to have a large tunable range by controlling the thickness and material composition of the IF layers. Our model provides an efficient tool for the designs of novel photodetectors.

REPORT DOCUMENTATION PAGE (SF298)
(Continuation Sheet)

Continuation for Block 13

ARO Report Number   58141.13-EL-MUR
Electronic band structures and optical properties   ...

Block 13: Supplementary Note

Electronic band structures and optical properties of type-II superlattice photodetectors with interfacial effect

Peng-Fei Qiao,[1] **Shin Mou,**[2] **and Shun Lien Chuang**[1,*]

[1]*University of Illinois at Urbana-Champaign, Department of Electrical and Computer Engineering, 1406 West Green Street, Urbana, Illinois 61801, USA*
[2]*Currently with Air Force Research Lab, Wright Patterson AFB, OH 45433, USA*

[*]*s-chuang@illinois.edu*

Abstract: The electronic band structures and optical properties of type-II superlattice (T2SL) photodetectors in the mid-infrared (IR) range are investigated. We formulate a rigorous band structure model using the 8-band $\mathbf{k} \cdot \mathbf{p}$ method to include the conduction and valence band mixing. After solving the 8×8 Hamiltonian and deriving explicitly the new momentum matrix elements in terms of envelope functions, optical transition rates are obtained through the Fermi's golden rule under various doping and injection conditions. Optical measurements on T2SL photodetectors are compared with our model and show good agreement. Our modeling results of quantum structures connect directly to the device-level design and simulation. The predicted doping effect is readily applicable to the optimization of photodetectors. We further include interfacial (IF) layers to study the significance of their effect. Optical properties of T2SLs are expected to have a large tunable range by controlling the thickness and material composition of the IF layers. Our model provides an efficient tool for the designs of novel photodetectors.

OCIS codes: (040.5160) Photodetectors; (040.4200) Multiple quantum well; (160.1890) Detector materials; (160.4760) Optical properties.

References and links

1. G. A. Sai-Halasz, R. Tsu, and L. Esaki, "A new semiconductor superlattice," Appl. Phys. Lett. **30**, 651–653 (1977).
2. D. L. Smith and C. Mailhiot, "Proposal for strained type II superlattice infrared detectors," J. Appl. Phys. **62**, 2545–2548 (1987).
3. J. Faist, F. Capasso, D. L. Sivco, C. Sirtori, A. L. Hutchinson, and A. Y. Cho, "Quantum cascade laser," Science **264**, 553–556 (1994).
4. C. S. Kim, M. Kim, W. W. Bewley, J. R. Lindle, C. L. Canedy, J. Abell, I. Vurgaftman, and J. R. Meyer, "Corrugated-sidewall interband cascade lasers with single-mode midwave-infrared emission at room temperature," Appl. Phys. Lett. **95**, 231103 (2009).
5. J. V. Li, R. Q. Yang, C. J. Hill, and S. L. Chuang, "Interband cascade detectors with room temperature photovoltaic operation," Appl. Phys. Lett. **86**, 101102 (2005).
6. H. Mohseni, V. I. Litvinov, and M. Razeghi, "Interface-induced suppression of the Auger recombination in type-II InAs/GaSb superlattices," Phys. Rev. B **58**, 15378–15380 (1998).
7. E. Kane, "The $\mathbf{k} \cdot \mathbf{p}$ method," in *Physics of III-V Cmopounds*, Vol. 1 of Semiconductors and Semimetals, R. Willardson and A. Beer, eds. (Academic Press, New York, 1966), pp. 75–100.
8. J. M. Luttinger and W. Kohn, "Motion of electrons and holes in perturbed periodic fields," Phys. Rev. **97**, 869–883 (1955).

9. G. Liu and S. L. Chuang, "Modeling of Sb-based type-II quantum cascade lasers," Phys. Rev. B **65**, 165220 (2002).
10. S. L. Chuang, *Physics of Photonic Devices*, 2nd ed. (Wiley, New York, 2009), Chap. 4 and 9.
11. L.-W. Wang, S.-H. Wei, T. Mattila, A. Zunger, I. Vurgaftman, and J. R. Meyer, "Multiband coupling and electronic structure of $(InAs)_n/(GaSb)_n$ superlattices," Phys. Rev. B **60**, 5590–5596 (1999).
12. Y.-M. Mu and S. S. Pei, "Effects of anisotropic k.p interactions on energy bands and optical properties of type-II interband cascade lasers," J. Appl. Phys. **96**, 1866–1879 (2004).
13. S. Mou, J. V. Li, and S. L. Chuang, "Quantum efficiency analysis of InAs-GaSb type-II superlattice photodiodes," IEEE J. Quantum Electron. **45**, 737–743 (2009).
14. F. Szmulowicz, "Derivation of a general expression for the momentum matrix elements within the envelope-function approximation," Phys. Rev. B **51**, 1613–1623 (1995).
15. Y.-C. Chang and R. B. James, "Saturation of intersubband transitions in p-type semiconductor quantum wells," Phys. Rev. B **39**, 12672–12681 (1989).
16. E. O. Kane, "Band structure of indium antimonide," J. Phys. Chem. Solids **1**, 249–261 (1957).
17. P. O. Löwdin, "A note on the quantum-mechanical perturbation theory," J. Chem. Phys. **19**, 1396–1401 (1951).
18. C. S. Chang and S. L. Chuang, "Modeling of strained quantum-well lasers with spin-orbit coupling," IEEE J. Sel. Top. Quantum Electron. **1**, 218–229 (1995).
19. J. V. Li, C. J. Hill, J. Mumolo, S. Gunapala, S. Mou, and S. L. Chuang, "Midinfrared type-II InAs/GaSb superlattice photodiodes toward room temperature operation," Appl. Phys. Lett. **93**, 163505 (2008).
20. C. J. Hill, J. V. Li, J. M. Mumolo, and S. D. Gunapala, "MBE grown type-II MWIR and LWIR superlattice photodiodes," Infrared Phys. Techn. **50**, 187–190 (2007).
21. A. Khoshakhlagh, E. Plis, S. Myers, Y. D. Sharma, L. R. Dawson, and S. Krishna, "Optimization of InAs/GaSb type-II superlattice interfaces for long-wave ($\sim 8\mu m$) infrared detection," J. Cryst. Growth **311**, 1901–1904 (2009).
22. H. J. Haugan, G. J. Brown, L. Grazulis, K. Mahalingam, and D. H. Tomich, "Optimization of InAs/GaSb type-II superlattices for high performance of photodetectors," Physica E **20**, 527–530 (2004).
23. Y. Huang, J.-H. Ryou, R. D. Dupuis, A. Petschke, M. Mandl, and S. L. Chuang, "InAs/GaSb type-II superlattice structures and photodiodes grown by metalorganic chemical vapor deposition," Appl. Phys. Lett. **96**, 251107 (2010).
24. Y. Wei and M. Razeghi, "Modeling of type-II InAs/GaSb superlattices using an empirical tight-binding method and interface engineering," Phys. Rev. B **69**, 085316 (2004).
25. G. L. Bir and G. E. Pikus, *Symmetry and Strain-Induced Effects in Semiconductors* (Wiley, New York, 1974).
26. T. B. Bahder, "Analytic dispersion relations near the γ point in strained zinc-blende crystals," Phys. Rev. B **45**, 1629–1637 (1992).
27. T. E. Ostromek, "Evaluation of matrix elements of the 8×8 k·p Hamiltonian with k-dependent spin-orbit contributions for the zinc-blende structure of GaAs," Phys. Rev. B **54**, 14467–14479 (1996).
28. G. Dresselhaus, "Spin-orbit coupling effects in zinc blende structures," Phys. Rev. **100**, 580–586 (1955).
29. I. Vurgaftman, J. R. Meyer, and L. R. Ram-Mohan, "Band parameters for IIIV compound semiconductors and their alloys," J. Appl. Phys. **89**, 5815–5875 (2001).
30. C. G. Van de Walle, "Band lineups and deformation potentials in the model-solid theory," Phys. Rev. B **39**, 1871–1883 (1989).

1. Introduction

Antimony-based type-II superlattices (T2SLs) have attracted great interest from researchers due to their wide range of applications in optoelectronic devices for the past decades. Such periodic quantum structures were first proposed by L. Esaki [1] in 1977 and applied to infrared (IR) applications by Smith and Mailhiot [2] in 1987. The broken-gap band alignment in type-II heterojunctions allows a narrow effective band gap between the quantized conduction band (CB) and valence band (VB) states. Long optical transition wavelength up to mid-IR (3 μm to 30 μm) becomes achievable for interband transitions without resorting to intersubband transitions [3]. The type-II material system, a promising candidate for active layer designs in mid-IR optoelectronic devices, has recently demonstrated room temperature operation in both interband cascade lasers [4] and photodetectors [5]. Antimony-based III-V compound SLs have higher growth quality and uniformity than II-VI compounds such as HgCdTe alloys, and a large reduction of defects is expected. A large tunable range of operation wavelength can be obtained by varying layer thicknesses rather than precise control of mole compositions. Suppression of Auger recombination is also predicted in antimony-based T2SLs [6].

The $\mathbf{k} \cdot \mathbf{p}$ method [7–10] serves as an efficient model, which covers from material level, quantum structural level, up to the device level modeling. Despite the loss of atomistic details [11], this method is desirable for large-scale problems, long wavelength applications, and device modeling [9, 12, 13]. The band structure near high-symmetry extremum points (e.g. Γ, X, L) is solved through the perturbation theory, and the output information is accurate enough for simulating optoelectronic processes near the semiconductor band gap. The results from the $\mathbf{k} \cdot \mathbf{p}$ method can be readily used for device-level analysis and design. Our previous work has applied this method for the gain optimization in type-II quantum cascade lasers [9]. The calculated material gain spectra, which enter into the rate equations for light-emitting devices, allow for more accurate modeling of the light output vs. injection current (L-I) curves. We have also analyzed the T2SL photodetector performance [13] including the quantum efficiency and responsivity, based on an analytical drift-diffusion model with the input of the calculated absorption spectra.

In this paper, we formulate a rigorous model for band structures and optical properties using the 8-band $\mathbf{k} \cdot \mathbf{p}$ method. We derive the new 8-band momentum matrix elements for TE and TM polarizations. Our expressions, explicitly derived in terms of the envelope functions, are more straightforward than those by Szmulowicz [14] (which were expressed in terms of matrices of operators), and more general than those by Chang and James [15] (which were derived only for intersubband transitions in the valence band, ignoring the CB-VB mixing). Our results under the axial approximation [9] significantly simplify the computation and are readily applicable for modeling optical transitions with CB and VB mixing, while the ab-initio band structure models are not yet applied for modeling T2SL optical properties and device performance.

One challenge in the $\mathbf{k} \cdot \mathbf{p}$ modeling is the determination of the input bulk band edge parameters. The electron effective mass and the Luttinger parameters, which account for the hole effective masses, become sensitive parameters when modeling narrow gap materials, such as InAs and InSb [16]. Band edge parameters, which enter into the Hamiltonian formulation, need to be corrected from experimental values. Such correction is only necessary for the 8-band $\mathbf{k} \cdot \mathbf{p}$ method or beyond, since the CB-VB coupling is already included in the off-diagonal terms in the 8×8 Hamiltonian. The Luttinger parameters are also corrected due to the change of the definition for class-B states (remote bands) in the Löwdin's perturbation method [17]. In the 6-band case [18], s-like CB states are considered as "remote bands", while in the 8-band case [7], s-like CB states belong to the 8-fold bases in class-A states. We present the correction formulas and summarize the corrected parameters for commonly used type-II materials.

We verify our model using two different boundary conditions: Dirichlet and Periodic Boundary Conditions (DBC and PBC). Important optical properties such as absorption coefficient and spontaneous emission rate are calculated and compared with the experimental data. Our theoretical results on absorption and photoluminescence (PL) spectra agree very well with the optical measurements. The measured quantum efficiency (QE) spectra of a mid-wave and a long-wave infrared photodetectors [19, 20] serve as verifications of our model. We further demonstrate the doping-dependence of the T2SL optical properties. The light p-doping does not change the cutoff wavelength and slightly affects the quantum efficiency. This allows us the freedom to optimize T2SL detectors using different levels of p-doping.

Another challenge of modeling heterostructures is the determination of the band alignment, or the commonly used parameter: valence band offset (VBO). Variation in the measured VBO causes a large fluctuation in the modeled results for narrow-gap materials. The interfacial (IF) layers formed at the heterojunctions play an important role in the uncertainty of band alignments besides experimental errors. Previous modeling work mostly included the IF effect by adjusting the VBO values or using a graded potential profile. However, these approaches failed to account for the large IF lattice mismatch and the strain effect on the band structure and the optical properties. In this paper, we include actual IF layers in our model and demonstrate the

significance of the IF effect. IF layers are often used to study lattice mismatch and achieve strain balance [21–24]. Beyond previous studies, we predict with our model that one can obtain a large tunable range of optical properties by controlling the IF layer type and thickness.

2. Theoretical principles

2.1. The 8-band $\mathbf{k} \cdot \mathbf{p}$ method with the effective mass correction

In this paper, the band structure and optical properties of T2SLs are modeled with the 8-band $\mathbf{k} \cdot \mathbf{p}$ method, which is based on the Kane's formulation [7, 10], the Luttinger-Kohn (LK) model [8, 10] for degenerate bands, and the Pikus-Bir theory [10, 25] for strain effects. Due to the narrow band gap of type-II materials, it is necessary to use an 8-band coupled Hamiltonian to include the strong interaction among the 8 bands nearest to the band gap, namely the conduction band (CB), the heavy-hole (HH), the light-hole (LH), and the spin-orbit split-off (SO) bands, each with a double spin degeneracy. The 8×8 LK Hamiltonian built under these 8 bases are first block-diagonalized into two decoupled 4×4 upper and lower Hamiltonian matrices as [9]

$$H_{8\times8}^{LK} = \left[\begin{array}{cc} H_{4\times4}^{U}(k_t) & 0 \\ 0 & H_{4\times4}^{L}(k_t) \end{array} \right],$$ (1)

using the basis transformation from Eq. (A-3) to Eq. (A-4). The band structure is generally anisotropic in the transverse plane and depends on the direction of the transverse wave number $\mathbf{k}_t$. After the axial approximation, the Hamiltonian matrix elements and the envelope functions depend only on the magnitude of $\mathbf{k}_t$. The upper and lower 4×4 Hamiltonians are written explicitly in Eq. (A-1). The upper and lower eigen-states of the m- and n-th subbands can be written as a linear conbination of the new basis functions modulated by the envelope functions $g^{(i)}$ as,

$$\Psi_m^U(\mathbf{k}_t, \mathbf{r}) = \frac{e^{i\mathbf{k}_t \cdot \mathbf{r}_t}}{\sqrt{A}} \sum_{i=1}^{4} g_m^{(i)}(k_t, z)) |u_i\rangle,$$
$$\Psi_n^L(\mathbf{k}_t, \mathbf{r}) = \frac{e^{i\mathbf{k}_t \cdot \mathbf{r}_t}}{\sqrt{A}} \sum_{i=5}^{8} g_n^{(i)}(k_t, z)) |u_i\rangle.$$ (2)

The eigen-energies and eigen-states at a given k_t can then be solved from the matrix equation,

$$H_{4\times4}^{U}(k_t) \left[\begin{array}{c} g^{(1)}(k_t, z) \\ g^{(2)}(k_t, z) \\ g^{(3)}(k_t, z) \\ g^{(4)}(k_t, z) \end{array} \right] = E^U(k_t) \left[\begin{array}{c} g^{(1)}(k_t, z) \\ g^{(2)}(k_t, z) \\ g^{(3)}(k_t, z) \\ g^{(4)}(k_t, z) \end{array} \right],$$ (3)

for the upper Hamiltonian. Similar equation holds for the lower Hamiltonian $H_{4\times4}^{L}(k_t)$. At the zone center ($k_t = 0$), there is usually a dominant component among the envelope functions which the band can be named after. For wide band gap materials, the CBs are weakly coupled to the valence bands (VBs) and usually solved separately from the 6×6 Hamiltonian with VB mixing [18], and the weak CB-VB coupling is included in the effecitve mass. In the 8×8 Hamiltonian for narrow band gap materials, the electron effective mass in the diagonal matrix elements need to be corrected since the off-diagonal elements already include the coupling. The

corrected effective mass, denoted by m_c', enters into the eight diagonal matrix elements as,

$$\langle u_{1,5}|H_{8\times8}^{LK}|u_{1,5}\rangle =E_c+A_\varepsilon+\left(\frac{\hbar^2}{2m_0}+A'\right)(k_t^2+k_z^2)=E_c+A_\varepsilon+\frac{\hbar^2}{2m_c'}(k_t^2+k_z^2),$$

$$\langle u_{2,6}|H_{8\times8}^{LK}|u_{2,6}\rangle =E_v-P_\varepsilon-Q_\varepsilon-\frac{\hbar^2}{2m_0}\left[(\gamma_1+\gamma_2)k_t^2+(\gamma_1-2\gamma_2)k_z^2\right],$$

$$\langle u_{3,7}|H_{8\times8}^{LK}|u_{3,7}\rangle =E_v-P_\varepsilon+Q_\varepsilon-\frac{\hbar^2}{2m_0}\left[(\gamma_1-\gamma_2)k_t^2+(\gamma_1+2\gamma_2)k_z^2\right],$$

$$\langle u_{4,8}|H_{8\times8}^{LK}|u_{4,8}\rangle =E_v-P_\varepsilon-\Delta-\frac{\hbar^2}{2m_0}\gamma_1\left(k_t^2+k_z^2\right). \tag{4}$$

where E_c and E_v are the unstrained bulk CB and VB edges, and Δ is the spin-orbit split-off energy. A_ε, P_ε, and Q_ε are the strain contributions, which are expressed explicitly in Eq. (A-2).

The corrected effective mass can be written in terms of Kane's paramemter A', which includes the momentum matrix elements between the s-like CBs and remote bands with Γ_5 symmetry type [7].

$$A'=\frac{\hbar^2}{m_0^2}\sum_j^{\Gamma_5}\frac{|\langle S|p_x|u_j\rangle|^2}{E_c-E_j} \tag{5}$$

The original effective mass m_c, which can be obtained from experiments, describes the curvature of the eigen-energy dispersion. The expression [26, 27] for m_c can be derived by solving energy dispersion $E(k_t)$ near the zone center with expansion up to $O(k_t^2)$,

$$\frac{m_0}{m_c}=1+\frac{2m_0}{\hbar^2}A'+E_p\frac{E_g+2\Delta/3}{E_g(E_g+\Delta)}. \tag{6}$$

Therefore the correction of electron effective mass from the experimental values is written as,

$$\frac{m_0}{m_c'}=\frac{m_0}{m_c}-E_p\frac{E_g+2\Delta/3}{E_g(E_g+\Delta)}. \tag{7}$$

The Luttinger parameters obtained from experiments correspond to the Dresselhaus [28] definition, where the class-A states for Löwdin's perturbation method [17] use the 6-fold VB bases. However, for the 8-band LK Hamiltonian, the class-A states should be defined using the 8-fold bases [7, 26, 27] including the two s-like CBs. Therefore the extra coupling term between the s-like CB states and the p-like VB states needs to be subtracted from the original Luttinger parameters [7, 26–29],

$$\gamma_1=\gamma_1^L-\frac{E_p}{3E_g+\Delta},$$

$$\gamma_2=\gamma_2^L-\frac{1}{2}\left(\frac{E_p}{3E_g+\Delta}\right), \tag{8}$$

$$\gamma_3=\gamma_3^L-\frac{1}{2}\left(\frac{E_p}{3E_g+\Delta}\right).$$

The original and the corrected material parameters are shown in Table 1. Values are updated from [9] to include the corrections and the original parameters are within error margins in [29].

Table 1. Input material parameters for the 8-band $\mathbf{k} \cdot \mathbf{p}$ method

Parameter	Symbol (unit)	GaSb	InAs	InSb	AlSb
Lattice constant (Å)	a	6.0854	6.0522	6.4717	6.1297
Deformation potentials (eV)					
	a_c	-7.5	-5.08	-6.94	-4.5
	a_v	0.8	1	0.36	1.4
	b	-2	-1.8	-2	-1.35
Elastic stiffness constant (10^{11}dyne/cm^2)	C_{11}	8.842	8.329	6.847	8.769
Elastic stiffness constant (10^{11}dyne/cm^2)	C_{12}	4.026	4.526	3.735	4.341
Band gap at 0K (eV)	E_g	0.81	0.42	0.235	2.386
Band gap at 77K (eV)	E_g	0.80	0.407	0.227	2.374
Electron effective mass	m_c/m_0	0.0412	0.0224	0.0135	0.13
Corrected electron effective mass	m_c'/m_0	1.053	2.51	1.84	2.716
Luttinger parameters					
	γ_1^L	11.84	19.4	32.4	4.15
	γ_2^L	4.25	8.545	13.3	1.28
	γ_3^L	5.01	9.17	15.15	1.75
Corrected Luttinger parameters					
	γ_1	4.86	6.30	16.78	1.76
	γ_2	0.76	1.99	5.61	0.085
	γ_3	1.52	2.62	7.46	0.55
Optical matrix parameter (eV)	E_p	22.4	21.5	23.3	18.7
Spin-orbit split-off energy (eV)	Δ	0.81	0.38	0.81	0.65
Valence-band offset energy (w.r.t. GaSb) (eV)	VBO	0	-0.56±0.01	0.03	-0.38

2.2. Dirichlet boundary condition (DBC) vs. periodic boundary condition (PBC)

Let the thickness of one superlattice period be L_p and the total thickness with N periods be $L_T = NL_p$. With DBC, the solution region is L_T and the wave functions at both ends are set to zero, or equivalently introducing infinite potential barriers outside the solution region.

$$g_m^{(i)}(k_t, -L_T/2) = g_m^{(i)}(k_t, L_T/2) = 0 \qquad (9)$$

With PBC, the solution region is L_p and the wave function values at both ends are related by Bloch's theorem. An extra quantum number q is introduced as a Bloch wave number $q\hat{z}$ to account for the superlattice periodicity in z-direction. The PBC is formulated as,

$$\begin{cases} g_m^{(i)}(k_t, z+L_p) = e^{iqL_p} g_m^{(i)}(k_t, z), \\ g_m^{(i)}(k_t, z+L_T) = g_m^{(i)}(k_t, z+NL_p) = g_m^{(i)}(k_t, z). \end{cases} \qquad (10)$$

The eigen-equation is obtained as,

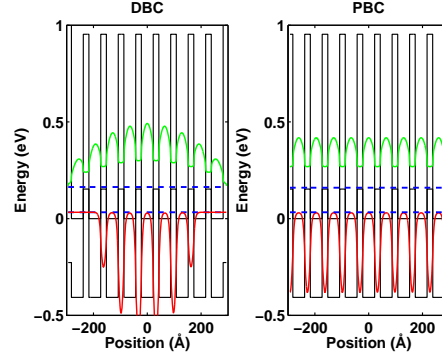$$e^{iNqL_p} = 1, \text{ and } q = \frac{2\pi n}{NL_p}. \qquad (11)$$

Fig. 1. Wavefunctions at $k_t = 0$ solved using the Dirichlet boundary condition (DBC) and the periodic boundary condition (PBC). $|g^{(1)}|$ of the lowest C1 band (green) and $|g^{(2)}|$ of the highest HH1 band (red) are plotted with C1 and HH1 band edges (blue dashed). The zero energy reference is chosen as the unstrained conduction band edge of InAs.
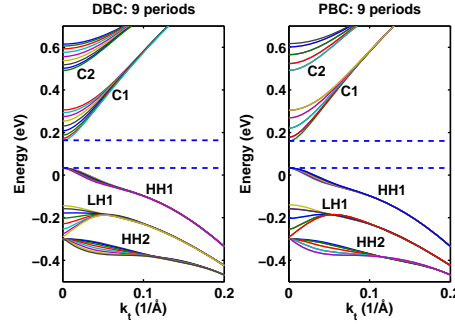

Fig. 2. Energy dispersion relation to transverse wave number. Blue dashed lines indicate the band edge energies. The zero energy reference is chosen as the unstrained conduction band edge of InAs.

where q takes N (or $N+1$) values in the first Brillouin zone $(-\pi/L_p, \pi/L_p)$,

$$
n = \begin{cases} 0, \pm 1, \pm 2, ..., \pm \dfrac{N}{2} & \text{N is even,} \\[2mm] 0, \pm 1, \pm 2, ..., \pm \dfrac{N-1}{2} & \text{N is odd.} \end{cases} \tag{12}
$$

The solution region of L_p is solved for N (or $N+1$) times with different Bloch phase shift determined by q. The number of unknowns for PBC is N (or $N+1$) times fewer than that of DBC but the eigen-problem is solved for N (or $N+1$) times. Since most eigen-solvers have a complexity greater than $O(N^2)$, the computational cost using PBC is much less than DBC when N becomes large.

After choosing the boundary condition, the coupled eigen-equations in Eq. (3) are solved numerically using the finite-difference method. Using DBC, each subband (e.g. C1 or HH1) is splitted into N coupled states, which is consistent with the coupled-mode theory. The band edge energies converge as N increases. Using PBC, the band edge is determined by the $q = 0$ states, where wavefunctions in one period are repeated in other periods without any phase change.

The dominant envelope functions ($g^{(1)}$ for CB, $g^{(2)}$ for HH) are plotted in Fig. 1. The zero

energy reference is chosen as the unstrained conduction band edge of InAs. Comparing DBC and PBC, band edge energies (blue dashed) agree well. The thin GaSb layers cause strong coupling between electrons confined in the InAs layers. For DBC, this strong coupling brings forth a slow-varying envelope that modulates CB wavefunctions, which is mathematically caused by the infinite barriers at both ends. For PBC, the strong coupling effect is reflected in the large non-zero mean value of the wavefunctions, even though the magnitude of the wavefunctions repeats for all periods. Despite the difference in wavefunctions, the optical transition matrices for DBC and PBC should converge, because the overlap integration can be approximately separated into a product of two integrals, one over fast-varying part in a single period of SL, and the other over the slow-varying part across the whole solution region. The average of the slow-varying envelope is equivalent to the large non-zero mean when using PBC.

The energy dispersion relations $E(k_t)$ are shown in Fig. 2, calculated using 9 periods of SLs. The assignment of the HH or LH band names is according to the dominant envelope function at the band edge (i.e. $g^{(2)}$ for HH and $g^{(3)}$ for LH). The effective band gap and the band edge energies for DBC and PBC agree well. For DBC, each subband is split into 9 coupled states, which converge at higher k_t. For PBC, each subband is split into 5 discrete energy levels because of the double degeneracy among the 9 different q values ($E^{+q}(k_t) = E^{-q}(k_t)$).

2.3. Absorption and photoluminescence spectra

The optical absorption coefficient [10] in a quantum well structure can be derived from the Fermi's golden rule and expressed as,

$$
\begin{aligned}
\alpha(\hbar\omega) = & \frac{\pi e^2}{n_r c \varepsilon_0 m_0^2 \omega} \sum_{\sigma_1, \sigma_2}^{U,L} \sum_{n,m} \frac{1}{L_T} \int_0^{2\pi} \frac{d\phi}{2\pi} \int_0^{\infty} \frac{k_t dk_t}{2\pi} |\langle \Psi_c^{\sigma_1,n} | \hat{e} \cdot \mathbf{p} | \Psi_v^{\sigma_2,m} \rangle|^2 \\
& \times [f_v^{\sigma_2,m}(k_t) - f_c^{\sigma_1,n}(k_t)] L(k_t, \hbar\omega),
\end{aligned}
\tag{13}
$$

where the Fermi distribution functions are

$$
\begin{aligned}
f_c^n(k_t) &= \frac{1}{1 + \exp(\frac{E_{c,n}(k_t) - F_c}{kT})}, \\
f_v^m(k_t) &= \frac{1}{1 + \exp(\frac{E_{v,m}(k_t) - F_v}{kT})}.
\end{aligned}
\tag{14}
$$

for electron occupation probability in the n-th conduction subband with an energy $E_{c,n}(k_t)$ and the m-th valence subband with an energy $E_{v,m}(k_t)$, respectively. F_c is the quasi-Fermi level for the conduction band electrons and F_v is the quasi-Fermi level for the valence band. $(1 - f_v^m)$ is the occupation probability by the holes. The summation over σ_1 and σ_2 includes the transitions among eigen-states of both upper and lower 4×4 Hamiltonian, and the spin degeneracy is also accounted for.

Evaluation of the 8×8 momentum matrix elements, as suggested by Chang and James [15], and Szmulowicz [14], is different from that of the 6×6 case [18], where the mixing among VB states is included but not the mixing between the CB and the VB states. In the 6×6 case, all interband transition matrix elements are proportional to $\langle S|p_z|Z\rangle$ since the CB states are purely s-like and the VB states are mixtures of p-like states. In the 8×8 case, both the CB and the VB states include the 8-band mixing and interband transition is allowed from p-like to p-like states. Such a transition (e.g. $\langle Z|p_z|Z\rangle$) is non-vanishing when Löwdin's perturbation method [17] is applied to include the remote bands denoted as class-B. Since the momentum operator does not commute with the Hamiltonian, even the new bases $\{|u_i\rangle\}$ cannot simultaneous block-diagonalize the momentum matrix. Such a dense 8×8 momentum matrix can be obtained from

the Hamiltonian using the $1st$-order $\mathbf{k} \cdot \mathbf{p}$ perturbation,

$$\mathbf{p}_{8\times8} = \frac{m_0}{\hbar}\nabla_{\mathbf{k}}H_{8\times8}, \tag{15}$$

since $H_{\mathbf{k}} \approx H_0 + (\hbar/m_0)\mathbf{k}\cdot\mathbf{p}$. The gradient in Eq. (15) is expanded by the $2nd$-order derivatives of the Hamiltonian. Then the momentum matrix elements can be written as,

$$\langle \Psi_c^{\sigma_1,n}(\mathbf{k}_t,z)|\hat{e}\cdot\mathbf{p}|\Psi_v^{\sigma_2,m}(\mathbf{k}_t,z)\rangle = \hat{e}\cdot\sum_{i,j}\int dz \left(g_n^{(i)}(k_t,z)\right)^* \left[\frac{m_0}{\hbar}\nabla_{\mathbf{k}}H_{ij}\right]g_m^{(j)}(k_t,z), \tag{16}$$

which is consistent with [15] and [14]. We further derive explicitly the 8×8 momentum matrix elements for TE and TM polarizations in terms of the envelope functions in Appendix B.

The direction $\hat{z}$ is chosen as the epitaxial growth direction of the T2SLs. Therefore in Eq. (16), $\hat{e}\perp\hat{z}$ and $\hat{e}\|\hat{z}$ for TE- and TM-polarized optical transitions, respectively. For mid-IR absorption spectra, TE polarization is of main interest because of its major contribution among top-incident light, especially near transition band edge, where normally HH1-C1 is dominating.

The lineshape function $L(k_t, \hbar\omega)$ uses the normalized Gaussian distribution to account for a finite transition linewidth due to various scattering mechanisms, with γ being the linewidth parameter,

$$L(k_t,\hbar\omega) = \frac{1}{\gamma\sqrt{2\pi}}\exp\left(-\frac{(E_{c,n}(k_t) - E_{v,m}(k_t) - \hbar\omega)^2}{2\gamma^2}\right). \tag{17}$$

Unlike absorption or stimulated emission where the net transition rate is calculated, spontaneous emission considers only the downward transition from the CBs to the VBs. It only requires the initial state to be occupied and the final state empty, assured by the term $f_c(1-f_v)$. The photoluminescence (PL) spectrum is proportional to the spontaneous emission spectrum,

$$r_{spon}(\hbar\omega) = \frac{n_r e^2 \omega}{c^3 \pi \hbar \varepsilon_0 m_0^2}\sum_{\sigma_1,\sigma_2}^{U,L}\sum_{n,m}\frac{1}{L_T}\int_0^{2\pi}\frac{d\phi}{2\pi}\int_0^{\infty}\frac{k_t dk_t}{2\pi}$$
$$|\langle\Psi_c^{\sigma_1,n}|\hat{e}\cdot\mathbf{p}|\Psi_v^{\sigma_2,m}\rangle|^2 f_c^{\sigma_1,n}(k_t)[1-f_v^{\sigma_2,m}(k_t)]L(k_t,\hbar\omega). \tag{18}$$

The integrations over k_t in Eq. (13) and (18) are performed numerically by truncating at a finite range ($k_t = 0.2/\text{Å}$). The lineshape function approaches zero rapidly when k_t is large, which indicates the high-k_t transitions contribute little to the infrared absorption or emission. For absorption in an intrinsic T2SL, the quasi Fermi-level separation is zero ($F_c = F_v$) and the Fermi-level lies in the middle of effective band gap. Therefore the Fermi function difference ($f_v - f_c$) is 1. For PL, low-level injection creates a small quasi Fermi-level separation but the two quasi Fermi-levels are both deep within the gap. For gain spectrum, the population inversion condition requires negative Fermi function difference ($f_v - f_c < 0$) in order to have a positive gain value. Therefore the injection level needs to be high enough to create a large quasi Fermi-level separation ($F_c - F_v$). Gain is equal to negative absorption,

$$g(\hbar\omega) = -\alpha(\hbar\omega). \tag{19}$$

For both PL and gain modeling, F_c and F_v are related to the injected carrier density by,

$$n = \sum_{\sigma_1}^{U,L}\sum_n\frac{1}{2\pi L_T}\int_0^{\infty}k_t dk_t f_c^{\sigma_1,n}(k_t),$$

$$p = \sum_{\sigma_2}^{U,L}\sum_m\frac{1}{2\pi L_T}\int_0^{\infty}k_t dk_t\left[1-f_v^{\sigma_2,m}(k_t)\right]. \tag{20}$$

To solve F_c and F_v using Eq. (20), we obtain carrier densities n and p from the charge neutrality condition,

$$n + N_A^- = p + N_D^+, \tag{21}$$

where N_A^- is the ionized acceptor concentration, N_D^+ is the ionized donor concentration. The carrier densities n and p can be found from $n = n_0 + \delta n$, $p = p_0 + \delta p$, and $\delta n = \delta p$, where n_0 and p_0 are the electron and hole concentrations, respectively, at thermal equilibrium. δn and δp are the excess electron and hole concentrations due to electrical or optical injection. For PL or low-level injection condition,

$$
\begin{aligned}
&n_0 = \frac{n_i^2}{p_0} \ll \delta n = \delta p \ll p_0 = N_A^- - N_D^+, && \text{for p-type,} \\
&p_0 = \frac{n_i^2}{n_0} \ll \delta n = \delta p \ll n_0 = N_D^+ - N_A^-, && \text{for n-type,} \\
&n_0 = p_0 = n_i \ll \delta n = \delta p, && \text{for intrinsic.}
\end{aligned}
\tag{22}
$$

For absorption spectra at zero bias, the excess carrier injection is zero ($\delta n = \delta p = 0$).

3. Simulation results and discussion

In this paper, we model the absorption spectrum and the PL spectrum for an intrinsic T2SL with an InAs/GaSb 44 Å/21 Å layer structure. Specific interband transitions (e.g. HH1-C1, LH1-C1) are calculated together with the total transition as shown in the inset of Fig. 3. The cutoff energies for different types of interband transitions are consistent with the effective band gaps between different subbands predicted from Fig. 2. The HH1-C1 transition turns on at around 130 meV in Fig. 3. The HH1-C2 transition appears at the second step of the HH1-to-all CBs absorption curve (black curve in Fig. 3 inset), which agrees with the effective band gap between C2 and HH1 subbands (470 meV) in Fig. 2. The LH1-C1 starts at around 300 meV, which is the effective band gap between C1 and LH1 subbands. The peak of LH1-C1 transition appears at 500 meV due to the large wavefunction overlap at this transition energy and the contribution from higher k_t states.

The external quantum efficiency (QE) of an InAs/GaSb 45 Å/24 Å T2SL photodetector is modeled with different p-doping conditions, as shown in Fig. 4. We use a uniform doping in the absorber, which can be well controlled during crystal growth. When the absorber region is lightly p-doped, the quantum efficiency decreases slightly because more holes are introduced in the VB. But the PL intensity increases with p-doping since the VB becomes increasingly occupied by holes (the quasi Fermi-level for holes shifts to lower energy), and allows a larger spontaneous emission rate. Since the doping is light and uniform, the problem of band distortion should not be significant. The fact that the light p-doping does not change the cutoff wavelength and only slightly affects the QE, one can use a lightly doped absorber region to reduce the dark current and drastically improve the electrical performance of photodetectors.

Our theoretical results are compared with the experimental data in Fig. 5 and Fig. 6, showing a very good agreement. The measured absorption spectra are converted from the quantum efficiency (QE) spectra [19, 20] for a mid-wave infrared (MWIR) detector with a 3.6 μm cutoff wavelength and a long-wave infrared detector (LWIR) with a 12 μm cutoff wavelength. The absorption coefficient is an intrinsic property of the designed T2SL while quantum efficiency is a device-dependent property, which can be affected by doping concentration, device thickness, minority carrier lifetime, minority carrier diffusion length, and so on. The absorption coefficient can be measured from the absorption difference between two identical T2SLs except with
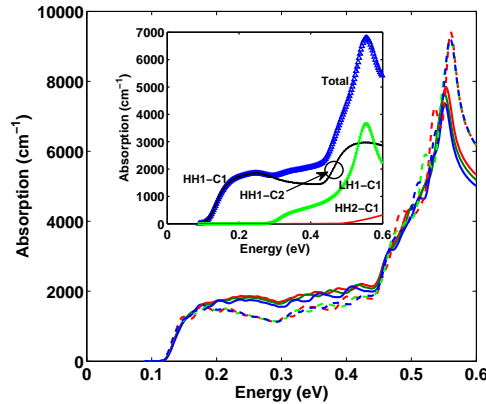
Fig. 3. Theoretical TE absorption spectra of an InAs/GaSb 44 Å/21 Å T2SL on GaSb substrate using Dirichlet boundary condition (DBC) with 7 (blue solid), 9 (green solid), and 11 (red solid) periods, and using the periodic boundary condition (PBC) with 11 (red dashed), 15 (green dashed), and 19 (blue dashed) periods. Inset: Total absorption (blue), first heavy-hole (HH1) to all conduction subbands (CBs) absorption (black), first light-hole (LH1) to all CBs absorption (green), and second heavy-hole (HH2) to all CBs absorption (red).
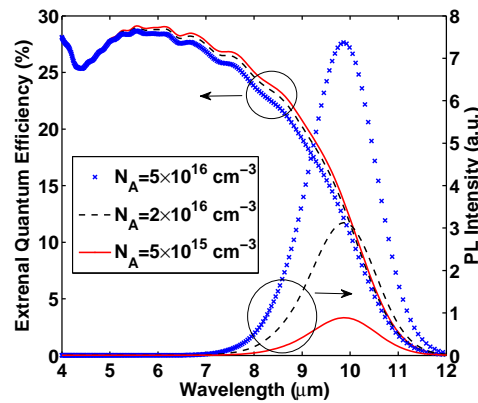

Fig. 4. Modeled external quantum efficiency and photoluminescence (PL) spectra of a 300-period lightly p-doped InAs/GaSb 45 Å/24 Å T2SL absorber with $N_A = 5 \times 10^{16}$ cm^{-3} (cross), $N_A = 2 \times 10^{16}$ cm^{-3} (dashed), $N_A = 5 \times 10^{15}$ cm^{-3} (solid).

different thicknesses, and the calibration is automatically included during the spectral response subtraction. The minor spectral dips in the measured QE spectra in Fig. 5 and Fig. 6 are due to the atmospheric absorption. The absorption data converted from measured QE follows our theoretical prediction for both MWIR and LWIR cases. The error becomes larger when wavelength approaches cutoff partially due to the increasing difficulty in separating weak signal from large noise fluctuation during measurement.

Small variations in material parameters and the layer structure become critical when modeling optical properties at long wavelength. A slight fluctuation in the input parameters, such as the layer thicknesses and the valence band offset (VBO), can cause a large percentage change with respect to the small transition energy. In LWIR range, even 5 meV change in the VBO results in nearly 1 μm shift in cutoff wavelength, as shown in Fig. 6.
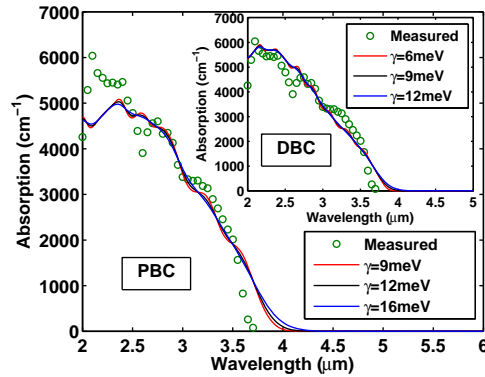
Fig. 5. Comparison between theoretical model and experimental data [19] for an InAs/GaSb 18 Å/22 Å MWIR T2SL on GaSb substrate. Both the periodic boundary condition (PBC) and Dirichlet boundary condition (DBC) (inset) are used, along with different linewidth parameter γ.
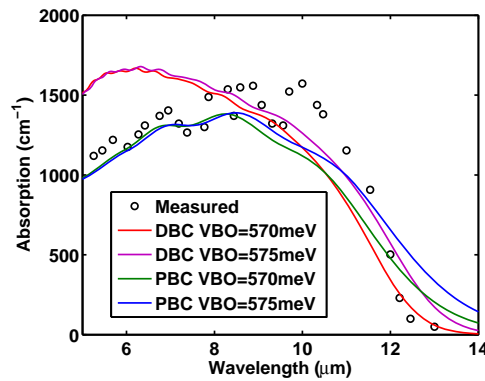

Fig. 6. Comparison between our theoretical model and experimental data [20] for an InAs/GaSb 48 Å/22 Å LWIR T2SL on GaSb substrate. Both the periodic boundary condition (PBC) and Dirichlet boundary condition (DBC) are used and different valence band offset (VBO) values take into account the interfacial effect if actual interfacial layers are not included in the model.

One major difficulty of modeling semiconductor nanostructures with heterojunctions is the determination of the band alignment and the VBO. One commonly used method is the model-solid theory [30], where the unstrained valence band edges for all materials are measured from an absolute reference. However, a large variation exists among reported experimental VBO values obtained through different measuring techniques or by different researchers. Besides experimental error, one of the major reasons is the imperfectness of the heterojunction formed in practice. Interfacial layers are formed unintentionally at the heterojunction and will affect the measurement of VBO and other optical properties.

In this paper, we include actual IF layers in our model to study their effect on optical properties. IF layers are forced at the heterojunction while the thickness of one superlattice period remains the same. If the interfacial type between InAs and GaSb is InSb, the unstrained CB edge for InSb is in between that of InAs and GaSb, and the unstrained VB edge is slightly higher than that of GaSb, as shown in Fig. 7 inset. However, due to the large lattice mismatch ($\sim 6\%$) between InSb layer and GaSb substrate, the strain effect plays an important role in the
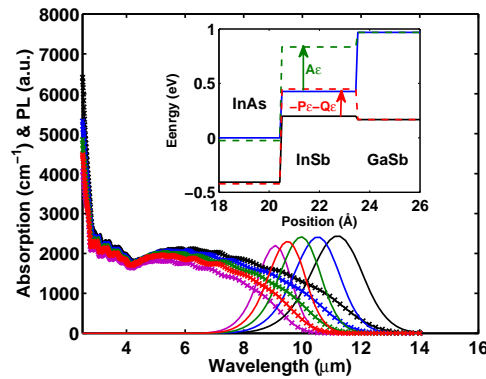
Fig. 7. Modeled TE absorption (cross) and PL (solid) spectra for InAs/GaSb 44 Å/21 Å T2SL on GaSb substrate when including InSb interfacial layers of different thicknesses: 0 Å (purple), 1 Å (red), 1.5 Å (green), 2 Å (blue), 2.5 Å (black). The inset shows the band edge profile at InAs/GaSb interface with forced InSb layer in between. The blue and black lines are unstrained conduction band and valence band edges respectively. The green and red dashed lines are conduction and heavy-hole band edges respectively including strain effect.

band alignment. The large biaxial compressive strain shifts the CB edge in InSb higher by 377 meV, and also shifts the HH edge higher by 230 meV.

Assuming pure InSb IF layers can be intentionally grown between the InAs and GaSb layers, the VB states in the T2SL are shifted to higher energies since the VB edge in InSb is much higher than the VB edges in both InAs and GaSb. The change in the CB state energies is small compared to the change in the VB state energies because the CB edge in InSb is still between the CB edges in InAs and GaSb. As a result, the InSb IF layer shrinks the effective band gap and increases the transition wavelength. Such effect can be observed from the red-shift of the PL peak and the absorption cutoff wavelength in Fig. 7. In our model, we include IF layers at both InAs-on-GaSb and GaSb-on-InAs interfaces. Practically, depositing InSb on InAs interfaces is much harder than that on GaSb. If the IF layer is only deposited on one type of interfaces, the effect of wavelength shift becomes approximately half of that on both interfaces.

There is normally a tradeoff between the cutoff wavelength and the absorption strength when designing T2SL, but the InSb IF layers are able to simultaneously increase both properties, as shown in Fig. 7. The absorption coefficient increases with InSb IF layer thickness because it improves the wavefunction overlap between electrons and holes. Electrons tunnel more easily through the interface and the hole-confining regions are effectively wider. As a result, the InSb IF layer becomes a preferable region for electrons and holes to recombine. In reality, GaAs or even ternary and quaternary compound IF layers can also be forced intentionally or formed unintentionally during the crystal growth of the InAs/GaSb T2SL. Due to the large biaxial tensile strain in GaAs on GaSb substrate, optical properties are affected in the opposite way as by InSb IF layers. A wide tunable range of optical properties can be achieved by controlling both the composition and the thickness of the IF layers.

4. Conclusion

We have presented a comprehensive model of the electronic band structure and optical properties of T2SL photodetectors using the 8-band $\mathbf{k} \cdot \mathbf{p}$ method. The theoretical formulation for the 8-band Hamiltonian and the explicit expressions of the 8-band momentum matrix elements are

included. Material parameters of Sb-based binary compounds commonly used in type-II structures are updated and summarized. Numerical results using two different boundary conditions are compared, showing good agreement. Our theoretical results of the T2SL optical properties, including the absorption and photoluminescence spectra, agree very well with the experimental data. Our model also explains well the doping-dependence of the quantum efficiency and photoluminescence in T2SL photodetectors.

The interfacial (IF) effect in T2SLs is investigated using our model. Instead of adjusting VBO to account for the IF effect, we include the actual IF layers in our model. IF layers are shown to have a large influence on the optical properties in T2SLs. It is predicted that by precise control of the IF layer component and thickness, we can achieve a large tunable range of the optical properties in T2SLs and significant improvement of the T2SL device performance.

A. The 8×8 Luttinger-Kohn Hamiltonian in the $\mathbf{k} \cdot \mathbf{p}$ method

After the basis transformation and axial approximation, the upper and lower parts of the block-diagonalized Hamiltonian [9] can be written as,

$$
H_{4\times4}^{U} = \begin{bmatrix}
E_c + A & -\sqrt{3}V_\rho & -V_\rho + i\sqrt{2}U & -\sqrt{2}V_\rho - iU \\
-\sqrt{3}V_\rho & E_v - P - Q & R_\rho + iS_\rho & \sqrt{2}R_\rho - i\frac{1}{\sqrt{2}}S_\rho \\
-V_\rho - i\sqrt{2}U & R_\rho - iS_\rho & E_v - P + Q & -\sqrt{2}Q - i\sqrt{\frac{3}{2}}S_\rho \\
-\sqrt{2}V_\rho + iU & \sqrt{2}R_\rho + i\frac{1}{\sqrt{2}}S_\rho & \sqrt{2}Q + i\sqrt{\frac{3}{2}}S_\rho & E_v - P - \Delta
\end{bmatrix},
$$

$$
H_{4\times4}^{L} = \begin{bmatrix}
E_c + A & -\sqrt{3}V_\rho & -V_\rho - i\sqrt{2}U & -\sqrt{2}V_\rho + iU \\
-\sqrt{3}V_\rho & E_v - P - Q & R_\rho - iS_\rho & \sqrt{2}R_\rho + i\frac{1}{\sqrt{2}}S_\rho \\
-V_\rho + i\sqrt{2}U & R_\rho + iS_\rho & E_v - P + Q & -\sqrt{2}Q + i\sqrt{\frac{3}{2}}S_\rho \\
-\sqrt{2}V_\rho - iU & \sqrt{2}R_\rho + i\frac{1}{\sqrt{2}}S_\rho & \sqrt{2}Q - i\sqrt{\frac{3}{2}}S_\rho & E_v - P - \Delta
\end{bmatrix},
$$

(A-1)

where

$$
A = \frac{\hbar^2}{2m_c'}(k_t^2 + k_z^2) + A_\varepsilon, \quad A_\varepsilon = a_c(\varepsilon_{xx} + \varepsilon_{yy} + \varepsilon_{zz}),
$$

$$
P = \frac{\hbar^2}{2m_0}\gamma_1(k_t^2 + k_z^2) + P_\varepsilon, \quad P_\varepsilon = -a_v(\varepsilon_{xx} + \varepsilon_{yy} + \varepsilon_{zz}),
$$

$$
Q = \frac{\hbar^2}{2m_0}\gamma_2(k_t^2 - 2k_z^2) + Q_\varepsilon, \quad Q_\varepsilon = -\frac{b}{2}(\varepsilon_{xx} + \varepsilon_{yy} - 2\varepsilon_{zz}),
$$

$$
R_\rho = -\frac{\hbar^2}{2m_0}\sqrt{3}\left(\frac{\gamma_2 + \gamma_3}{2}\right)k_t^2 = -\frac{\hbar^2}{2m_0}\sqrt{3}\bar{\gamma}k_t^2, \quad \text{(A-2)}
$$

$$
S_\rho = \frac{\hbar^2}{2m_0}2\sqrt{3}\gamma_3 k_t^2, \quad V_\rho = \frac{1}{\sqrt{6}}P_{cv}k_t, \quad U = \frac{1}{\sqrt{3}}P_{cv}k_z,
$$

$$
P_{cv} = \frac{\hbar}{m_0}\langle iS|\frac{\hbar}{i}\frac{\partial}{\partial x}|X\rangle = \sqrt{(\hbar^2/2m_0)E_p},
$$

$$
\varepsilon_{xx} = \varepsilon_{yy} = \frac{a_0 - a}{a}, \quad \varepsilon_{zz} = -\frac{2C_{12}}{C_{11}}\varepsilon_{xx},
$$

and m_c', γ_1, γ_2, γ_3 are the corrected electron effective mass and corrected Luttinger parameters based on experimental values and Eq. (7)-(8). P_{cv} is the Kane's parameter corresponding to the momentum matrix element for s-state to p-state interband transitions, which is also represented

by the energy parameter E_p. a_c, a_v, and b are the Pikus-Bir deformation potentials that introduce strain effect into the Hamiltonian. For quantum well structures, k_z is replaced by the differential operator $-i\partial/\partial z$ in the Hamiltonian.

The set of bases which block-diagonalizes the Hamiltonian is chosen as,

$$
\begin{aligned}
&|u_1\rangle = \frac{1}{\sqrt{2}}[|1\rangle e^{-i\phi/2} + i|5\rangle e^{i\phi/2}], &&|u_5\rangle = \frac{1}{\sqrt{2}}[|1\rangle e^{-i\phi/2} - i|5\rangle e^{i\phi/2}],\\
&|u_2\rangle = \frac{1}{\sqrt{2}}[|2\rangle e^{-i3\phi/2} - i|6\rangle e^{i3\phi/2}], &&|u_6\rangle = \frac{1}{\sqrt{2}}[|2\rangle e^{-i3\phi/2} + i|6\rangle e^{i3\phi/2}],\\
&|u_3\rangle = \frac{1}{\sqrt{2}}[i|3\rangle e^{-i\phi/2} - |7\rangle e^{i\phi/2}], &&|u_7\rangle = \frac{1}{\sqrt{2}}[-i|3\rangle e^{-i\phi/2} - |7\rangle e^{i\phi/2}],\\
&|u_4\rangle = \frac{1}{\sqrt{2}}[-i|4\rangle e^{-i\phi/2} - |8\rangle e^{i\phi/2}], &&|u_8\rangle = \frac{1}{\sqrt{2}}[i|4\rangle e^{-i\phi/2} - |8\rangle e^{i\phi/2}].
\end{aligned}
\tag{A-3}
$$

The original set of bases for the 8×8 LK Hamiltonian is:

$$
\begin{aligned}
&|1\rangle = |iS\uparrow\rangle, &&|5\rangle = |iS\downarrow\rangle,\\
&|2\rangle = -\frac{1}{\sqrt{2}}|(X+iY)\uparrow\rangle, &&|6\rangle = \frac{1}{\sqrt{2}}|(X-iY)\downarrow\rangle,\\
&|3\rangle = \frac{1}{\sqrt{6}}|-(X+iY)\downarrow+2Z\uparrow\rangle, &&|7\rangle = \frac{1}{\sqrt{6}}|(X-iY)\uparrow+2Z\downarrow\rangle,\\
&|4\rangle = \frac{1}{\sqrt{3}}|(X+iY)\downarrow+Z\uparrow\rangle, &&|8\rangle = \frac{1}{\sqrt{3}}|(X-iY)\uparrow-Z\downarrow\rangle.
\end{aligned}
\tag{A-4}
$$

B.   The 8×8 Momentum Matrix Elements

The 8×8 momentum matrix [14, 15] $\mathbf{p}$ can be derived from the 8×8 Hamiltonian under the same set of bases, following Eq. (15). Each energy eigen-state can be expressed in terms of basis functions weighted by envelope functions using $\mathbf{k}\cdot\mathbf{p}$ perturbation. The momentum matrix elements for the transitions between two energy eigen-states are then evaluated. Our contribution is to derive the general and explicit momentum matrix elements in terms of the envelope functions, which can be readily used after solving the coupled Hamiltonian. The results are shown as follows, where $\phi = \tan^{-1}(k_y/k_x)$.

$$
\begin{aligned}
\langle \Psi_c^{n,\sigma_1=U}|\hat{x}\cdot\mathbf{p}|\Psi_v^{m,\sigma_2=U}\rangle = \cos\phi \int dz \Bigg\{ &\hbar k_t[\frac{m_0}{m_c'}g_{1,n}^* g_{1,m} - (\gamma_1+\gamma_2)g_{2,n}^* g_{2,m} - (\gamma_1-\gamma_2)g_{3,n}^* g_{3,m}\\
&- \gamma_1 g_{4,n}^* g_{4,m} - \sqrt{3}\bar{\gamma}g_{2,n}^* g_{3,m} - \sqrt{6}\bar{\gamma}g_{2,n}^* g_{4,m} - \sqrt{3}\bar{\gamma}g_{3,n}^* g_{2,m} - \sqrt{6}\bar{\gamma}g_{4,n}^* g_{2,m} - \sqrt{2}\gamma_2 g_{3,n}^* g_{4,m}\\
&- \sqrt{2}\gamma_2 g_{4,n}^* g_{3,m}] - \frac{P_{cv}m_0}{\sqrt{6}\hbar}[\sqrt{3}g_{1,n}^* g_{2,m} + g_{1,n}^* g_{3,m} + \sqrt{2}g_{1,n}^* g_{4,m} + \sqrt{3}g_{2,n}^* g_{1,m} + g_{3,n}^* g_{1,m}\\
&+ \sqrt{2}g_{4,n}^* g_{1,m}] + \frac{\sqrt{3}\gamma_3\hbar}{2}[g_{2,n}^* \frac{d}{dz}g_{3,m} - g_{3,m}\frac{d}{dz}g_{2,n}^* - g_{3,n}^* \frac{d}{dz}g_{2,m} + g_{2,m}\frac{d}{dz}g_{3,n}^*]\\
&+ \frac{\sqrt{3}\gamma_3\hbar}{2\sqrt{2}}[g_{4,m}\frac{d}{dz}g_{2,n}^* - g_{2,n}^* \frac{d}{dz}g_{4,m} - g_{2,m}\frac{d}{dz}g_{4,n}^* + g_{4,n}^* \frac{d}{dz}g_{2,m}]\\
&+ \frac{3\gamma_3\hbar}{2\sqrt{2}}[g_{4,m}\frac{d}{dz}g_{3,n}^* - g_{3,n}^* \frac{d}{dz}g_{4,m} - g_{3,m}\frac{d}{dz}g_{4,n}^* + g_{4,n}^* \frac{d}{dz}g_{3,m}] \Bigg\}.
\end{aligned}
\tag{B-1}
$$

$\langle \Psi_c^{n,\sigma_1=L}|\hat{x}\cdot\mathbf{p}|\Psi_v^{m,\sigma_2=L}\rangle$ can be obtained by replacing $g_{i,n}$ with $g_{i+4,n}$, $g_{i,m}$ with $g_{i+4,m}$, and d/dz with $(-d/dz)$, based on Eq. (B-1).

$$\langle \Psi_c^{n,\sigma_1=U}|\hat{x}\cdot\mathbf{p}|\Psi_v^{m,\sigma_2=L}\rangle = i\sin\phi \int dz \Big\{ \hbar k_t [-\sqrt{3}\bar{\gamma}g_{2,n}^*g_{7,m} - \sqrt{6}\bar{\gamma}g_{2,n}^*g_{8,m} + \sqrt{3}\bar{\gamma}g_{3,n}^*g_{6,m}$$

$$+ \sqrt{6}\bar{\gamma}g_{4,n}^*g_{6,m}] + \frac{P_{cv}m_0}{\sqrt{6}\hbar}[\sqrt{3}g_{1,n}^*g_{6,m} - g_{1,n}^*g_{7,m} - \sqrt{2}g_{1,n}^*g_{8,m} - \sqrt{3}g_{2,n}^*g_{5,m} + g_{3,n}^*g_{5,m}$$

$$+ \sqrt{2}g_{4,n}^*g_{5,m}] + \frac{\sqrt{3}\gamma_3\hbar}{2}[g_{2,n}^*\frac{d}{dz}g_{7,m} - g_{7,m}\frac{d}{dz}g_{2,n}^* + g_{3,n}^*\frac{d}{dz}g_{6,m} - g_{6,m}\frac{d}{dz}g_{3,n}^*]$$

$$+ \frac{\sqrt{3}\gamma_3\hbar}{2\sqrt{2}}[g_{6,m}\frac{d}{dz}g_{4,n}^* - g_{4,n}^*\frac{d}{dz}g_{6,m} - g_{8,m}\frac{d}{dz}g_{2,n}^* + g_{2,n}^*\frac{d}{dz}g_{8,m}]$$

$$+ \frac{3\gamma_3\hbar}{2\sqrt{2}}[g_{8,m}\frac{d}{dz}g_{3,n}^* - g_{3,n}^*\frac{d}{dz}g_{8,m} - g_{7,m}\frac{d}{dz}g_{4,n}^* + g_{4,n}^*\frac{d}{dz}g_{7,m}] \Big\}.$$

$$(B\text{-}2)$$

$\langle \Psi_c^{n,\sigma_1=L}|\hat{x}\cdot\mathbf{p}|\Psi_v^{m,\sigma_2=U}\rangle$ can be obtained by replacing $g_{i,n}$ with $g_{i+4,n}$, $g_{i,m}$ with $g_{i-4,m}$, and d/dz with $(-d/dz)$, based on Eq. (B-2).

$$\langle \Psi_c^{n,\sigma_1=U}|\hat{z}\cdot\mathbf{p}|\Psi_v^{m,\sigma_2=U}\rangle = i\int dz \Big\{ -\frac{P_{cv}m_0}{\sqrt{3}\hbar}[\sqrt{2}g_{1,n}^*g_{3,m} - g_{1,n}^*g_{4,m} - \sqrt{2}g_{3,n}^*g_{1,m} + g_{4,n}^*g_{1,m}]$$

$$+ \sqrt{\frac{3}{2}}\gamma_3 k_t[\sqrt{2}g_{2,n}^*g_{3,m} - g_{2,n}^*g_{4,m} - \sqrt{2}g_{3,n}^*g_{2,m}] + g_{4,n}^*g_{2,m} - \sqrt{3}g_{3,n}^*g_{4,m} + \sqrt{3}g_{4,n}^*g_{3,m}]$$

$$- \frac{m_0}{2m_c'}[g_{1,n}^*\frac{d}{dz}g_{1,m} - g_{1,m}\frac{d}{dz}g_{1,n}^*] + \frac{\gamma_1 - 2\gamma_2}{2}[g_{2,n}^*\frac{d}{dz}g_{2,m} - g_{2,m}\frac{d}{dz}g_{2,n}^*]$$

$$+ \frac{\gamma_1 + 2\gamma_2}{2}[g_{3,n}^*\frac{d}{dz}g_{3,m} - g_{3,m}\frac{d}{dz}g_{3,n}^*] + \frac{\gamma_1}{2}[g_{4,n}^*\frac{d}{dz}g_{4,m} - g_{4,m}\frac{d}{dz}g_{4,n}^*] \Big\},$$

$$\langle \Psi_c^{n,\sigma_1=U}|\hat{z}\cdot\mathbf{p}|\Psi_v^{m,\sigma_2=L}\rangle = 0,$$

$$\langle \Psi_c^{n,\sigma_1=L}|\hat{z}\cdot\mathbf{p}|\Psi_v^{m,\sigma_2=U}\rangle = 0.$$

$$(B\text{-}3)$$

$\langle \Psi_c^{n,\sigma_1=L}|\hat{z}\cdot\mathbf{p}|\Psi_v^{m,\sigma_2=L}\rangle$ can be obtained by replacing $g_{i,n}$ with $g_{i+4,n}$, $g_{i,m}$ with $g_{i+4,m}$, but not replacing d/dz with $(-d/dz)$, based on Eq. (B-3).

The y-polarized momentum matrix elements are different from the x-polarized ones only in the ϕ-dependent terms. However, after the ϕ-integration in Eq. (13), both x- and y- polarizations give the same TE transition rate.

$\langle \Psi_c^{n,\sigma_1=U}|\hat{y}\cdot\mathbf{p}|\Psi_v^{m,\sigma_2=U}\rangle$ can be obtained from the expression of $\langle \Psi_c^{n,\sigma_1=U}|\hat{x}\cdot\mathbf{p}|\Psi_v^{m,\sigma_2=U}\rangle$ by replacing $\cos\phi$ with $\sin\phi$.

$\langle \Psi_c^{n,\sigma_1=U}|\hat{y}\cdot\mathbf{p}|\Psi_v^{m,\sigma_2=L}\rangle$ can be obtained from the expression of $\langle \Psi_c^{n,\sigma_1=U}|\hat{x}\cdot\mathbf{p}|\Psi_v^{m,\sigma_2=L}\rangle$ by replacing $\sin\phi$ with $(-\cos\phi)$.

$\langle \Psi_c^{n,\sigma_1=L}|\hat{y}\cdot\mathbf{p}|\Psi_v^{m,\sigma_2=U}\rangle$ can be obtained from the expression of $\langle \Psi_c^{n,\sigma_1=L}|\hat{x}\cdot\mathbf{p}|\Psi_v^{m,\sigma_2=U}\rangle$ by replacing $\sin\phi$ with $(-\cos\phi)$.

$\langle \Psi_c^{n,\sigma_1=L}|\hat{y}\cdot\mathbf{p}|\Psi_v^{m,\sigma_2=L}\rangle$ can be obtained from the expression of $\langle \Psi_c^{n,\sigma_1=L}|\hat{x}\cdot\mathbf{p}|\Psi_v^{m,\sigma_2=L}\rangle$ by replacing $\cos\phi$ with $\sin\phi$.

Acknowledgments